AI-BASED MAPPING FOR NAVIGATION ON SIGNIFICANTLY UNSTRUCTURED PLANETARY SURFACES

A. Liesch*, P. Suwinski*, B. Liu*, V. Chernykh*, K. Janschek*

* Institute of Automation, Faculty of Electrical and Computer Engineering, TUD Dresden University of Technology, 01187 Dresden, Germany

Abstract

For the future exploration of our solar system, missions to Small Solar System Bodies (SSSBs), such as asteroids or comets, are a promising and scientifically important area. The current missions exploring SSSBs require extensive human monitoring and processing to ensure safe operations. By incorporating more onboard autonomy, spacecrafts can explore SSSBs more efficiently and increase scientific output. The Astrone project posed a novel concept of a low-altitude hovering vehicle directly on the surface of an SSSB. This paper presents the AI Mapping, as a part of the extension of the Astrone project's navigation concept with additional AI-based algorithms. The AI Mapping consists of two parts. First, an overview of the AI-based Light imaging, detection, and ranging (LiDAR)/Camera data fusion will be given. With this method, a resolution increase of low-resolution flash-LiDAR data by a factor 8×8 was achieved. Second, the obtained high-resolution data was used in addition to the corresponding wide-angle monocular 2D grayscale images of the irregular and unstructured surface of the SSSB to pre-identify possible landing sites. The Convolutional Neural Network (CNN)-based approach was trained and tested with our artificially generated data set. Different versions of the Deeplabv3+ with certain ResNet and ResNet-RS backbone nets were compared. The results show that hazardous areas such as rocks, boulders, and craters on the surface could be detected successfully. With this method, it was possible to achieve an Intersection over Union (IoU) of 67.45 for the semantic segmentation task.

NOMENCLATURE

Abbreviations

AI	Artificial Intelligence
CNN	Convolutional Neural Network
DEM	Digital Elevation Map
DN	Discrimantor Network
GAN	Generative Adversarial Network
GNC	Guidance Navigation and Control
GN	Generator Network
GPU	Graphics Processing Unit
IoU	Intersection over Union
LiDAR	Light imaging, detection and ranging
SCB	Small Celestial Body
SfS	Shape from Shading
SSSB	Small Solar System Body

1. INTRODUCTION

For the future exploration of our solar system, missions to SSSBs, such as asteroids or comets, are a promising and scientifically important area.

Exploring asteroids or comets can provide valuable insights into the genesis and progression of our solar system while also enabling us to identify lucrative resources for upcoming space missions. However, conducting exploration missions to SSSBs presents several challenges. Besides the small, varying gravity or the unstructured, irregular surface and landform, the long distances to Earth, particularly the impossible real-time communication between ground control and the exploring spacecraft, is one major problem. Current missions to the close vicinity of Small Celestial Bodies (SCBs) require plenty of human monitoring and processing to ensure a safe flight during the space exploration mission. Thus, the exploration of SSSBs is intrinsically tied to the achievement of autonomy within mission operations. As missions become more complex, either due to an increase in the number of probes or the exploration of multiple targets, the importance of autonomy is further underscored. Therefore, a spacecraft's capability to execute tasks and make decisions with minimal human interven-

tion is envisioned. To achieve this, the spacecraft's trajectory with respect to Earth has been tracked precisely through radiometric absolute navigation and optical relative navigation [1–4]. Landmark-based navigation has also aided in spacecraft localization and orientation by utilizing identifiable features on the SSSB's surface. Despite the success of these technologies, their reliance on continuous human monitoring and processing remains a limitation. A spacecraft capable of fully autonomous exploration would land and survey the entire area independently.

The recently finished Astrone [5] project proposed a novel concept of a low-altitude hovering vehicle directly on the surface of an SSSB like 67P/Churyumov–Gerasimenko that enables advanced surface mobility. To support the resulting Guidance, Navigation, and Control (GNC) System, we propose Artificial Intelligence (AI)-based Mapping to improve the navigation concept performance in the context of the current Astrone KI [6] project. This paper presents an overview of a GAN-based solution to provide a high-resolution depth image of the asteroid's or comet's surface by data fusion of low-resolution flash-LiDAR data and the corresponding high-resolution monocular grayscale 2D camera image. The availability of high-resolution data enables AI-based landing site detection to pre-identify suitable landing sites from even greater distances.

To summarize, the main contributions of this paper are as follows:
- overview of the AI-based flash-LiDAR / camera data fusion to enable the AI-based landing site detection [7],
- overview of the generated training and validation data for the AI-based landing site detection,
- CNN architecture, training setup, and validation results for a first landing site AI-based landing site detection.

2. RELATED WORK

In recent space missions, there has been a gradual integration of technology aimed at expanding the boundaries of autonomy. Hayabusa-2 [8], launched in 2014, utilized upgraded navigation tools and advanced characterization techniques such as radiometric tracking and autonomous descent. Similarly, the OSIRIS-REx mission [9], launched in 2016, utilized vision-based navigation for close-range operations and radiometric tracking while integrating advanced exposure techniques and landmark tracking. Most recently, DART3 [10] launched successfully in 2021 and achieved kinetic impact deflection using a fully autonomous navigation system and avionics. As we approach the limits of human intervention or ground-based control in SSSB missions, advancing the frontiers of autonomy in upcoming missions becomes increasingly imperative. Autonomy becomes crucial to ensure optimal performance, especially when oper-

ating at considerable distances where communication delays pose significant challenges. Envisioned scenarios include multiple spacecraft independently landing and exploring asteroid fields with minimal human intervention. To compensate for that, AI-based machine-learning approaches can be used.

Improved sensor capabilities also play a crucial role, allowing spacecraft to acquire precise and reliable data for autonomous operations. According to the previous Astrone project's exploration concept, we acquire data from a monocular grayscale camera and a flash-LiDAR sensor from an aerial position of the close SSSB's surface [6]. A flash-LiDAR-aided inertial navigation system has been developed and successfully tested in a simulated SSSB environment by Liu et al. (2021) [11]. But the relatively low-resolution 128×128 flash-LiDAR data is mainly the limiting factor for tasks like 3D terrain reconstruction. Therefore, this low-resolution data was fused by AI-based data fusion with the available high-resolution 1024×1024 2D grayscale image to increase the resolution of the flash-LiDAR data [7]. With that approach, only one single monocular grayscale 2D image could be used for the data fusion. Multiple images of the same scene taken under different illumination conditions to minimize slope determination are not required. This is essential for the Astrone exploration concept and one reason why Shape-from-Shading (SfS) based approaches [12, 13] with the necessity to take multiple images of the asteroid's or comet's surface under different illumination conditions are unsuitable following the Astrone exploration concept. The obtained high-resolution data can now be used for AI preprocessing tasks like semantic segmentation, volume center point prediction [14], and AI-based landing site detection.

3. CONCEPT OF AI-BASED MAPPING

The current Astrone navigation concept is shown in Fig. 1. The enhanced navigation concept of Astrone KI includes additional AI-based algorithms. Both AI-based and non-AI algorithms are used collaboratively as part of local navigation on the SSSB's surface and shown in Fig. 2. The AI pre-processing step was introduced by Suwinski et al. (2023) [14]. This paper focuses on the AI Mapping block. The current Astrone navigation solution provides a 3D surface map (extended DEM). However, the resolution of the map and, therefore, the detection range is limited by the resolution of the flash-LiDAR data. To eliminate this limitation, we use an AI-based approach for the complex task to increase the resolution by data fusion with the corresponding 2D monocular grayscale 2D camera image. A GAN approach was applied to early-fuse [15] these data and generate a high-resolution output. For the asteroid exploration mission, the results of the AI-based map generation from camera and flash-LiDAR data will enable long-distance hazards/landing site detection.
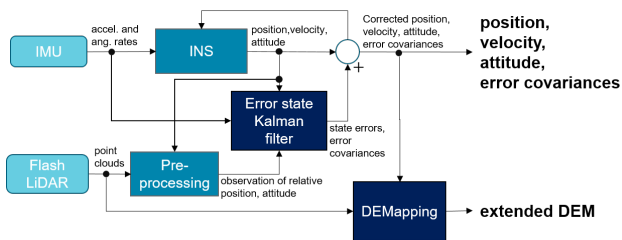
FIG 1. Astrone project's navigation concept [5, 6].

In addition, the AI-driven analysis solution to pre-identify suitable landing sites contains a CNN that processes the improved high-resolution flash-LiDAR data and grayscale 2D image in the camera frame. The CNN's input image resolution was assumed to be 256×256 instead of the computationally expensive 1024×1024 resolution we receive from our AI-based map generation. The unstructured and irregular surface of an asteroid or comet poses a challenge. Therefore, the main focus was to adapt suitable CNNs for semantic segmentation tasks. Open source available labeled datasets for supervised training of CNNs with realistic and usable 2D image and depth image data from asteroids or comets are rare. The synthetic dataset presented by Suwinski et al. (2023) [14] through the approach of Schmipf et al. (2022) [16] was used, inspired by the Rosetta orbiter mission's generated images of the 67P/Churyumov-Gerasimenko comet's surface [17].
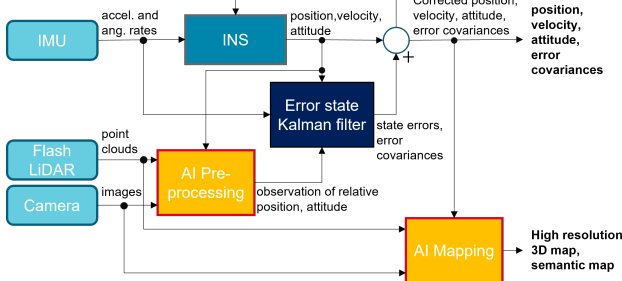

FIG 2. Astrone KI project's navigation concept including AI-algorithms.

3.1. AI-based LiDAR / Camera data fusion

The approach employs an advanced GAN architecture to create high-resolution data from low-resolution flash-LiDAR data by data fusion with a monocular grayscale 2D camera image. The GAN architecture was introduced by Goodfellow et al. (2014) [18]. During training, a generative network learns to produce data, while a Discriminator Network (DN) is trained to differentiate between generated and actual ground truth data. After training, only the generator part of the GAN is used to predict the output. This architecture has demonstrated its effectiveness in tasks like monocular depth estimation in recent works [19–21].

Our GAN consists of a Generator Network (GN) based on an advanced U-Net [22] architecture and a DN. The
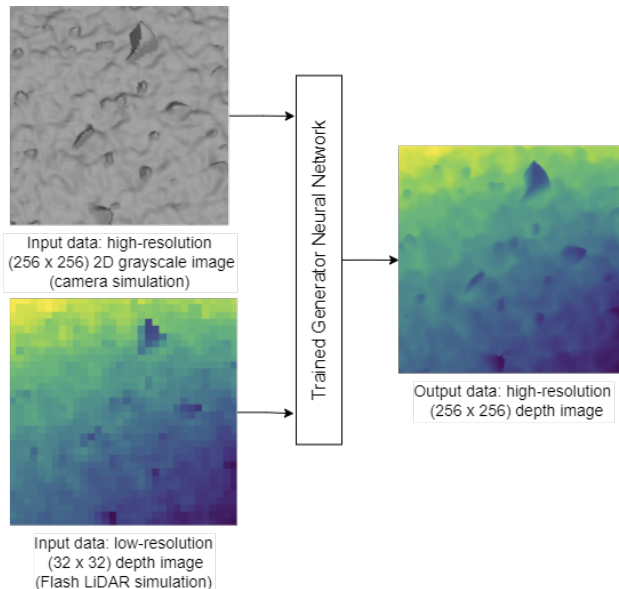

FIG 3. Qualitative input and output of the AI-based LiDAR/Camera data fusion for one tile of the complete input (128×128 depth and 1024×1024 grayscale image).

U-Net3+ [23] was applied as an advanced version of the original U-Net using full-scale skip connections as the GN. The network receives the flash-LiDAR data as depth images. The GN generates new data based on its input (low-resolution and camera data). During the training process, the GN was primarily taught to reconstruct low-frequency information. The challenge was to extract the high-frequency information of the irregular and unstructured surface. The CNN-based PatchGAN [24] was utilized as DN. This DN classifies its input as real (ground truth) or fake (GN's output). The PatchGAN DN does this for a 70×70 patch instead of classifying its input as one complete part. Structures at the scale of these patches are penalized. In this case, the DN has the task of restricting the model's high-frequency structures. Further, this approach enables possibilities to judge the validity of the GN's output concerning local regions. For processing, sparse depth images were created from the low-resolution data where missing values are set to 0. This was done to match the resolution of the input grayscale 2D image. Due to hardware limitations during training, the 2D image and sparse depth image with the dimension 1024×1024 had to be separated into 256×256 tiles to feed them into the GN. Each tile was processed individually by the GN. With this method, it was possible to increase the 128×128 low-resolution LiDAR data by 8×8 to a resolution of 1024×1024. For better visualization, Fig. 3 shows the input and output of the GN for one 256×256 tile with the corresponding 32×32 low-resolution input depth data.

3.2. AI-based landing site detection

We applied different versions of the CNN Deeplabv3+ [25] for comparable semantic segmentation tasks to the Astrone KI navigation concept. The tests in [14]

showed that the Deeplabv3+ outperforms other test candidates in the comparable Artificial Lunar Landscape Dataset.

The Deeplabv3+ can utilize different CNNs as a backbone net. The backbone net or encoder part extracts hierarchical features across various scales. This strategy enables the model to capture both global and local contextual information from the input pixel data. An Atrous Spatial Pyramid Pooling (ASPP) module is integrated into Deeplabv3+ to enhance segmentation accuracy. The ASPP module facilitates the model in perceiving fine-grained and larger scales, contributing to improved segmentation accuracy. The ASPP module achieves this by employing atrous dilated convolutions with multiple rates. These convolutions capture context information at different receptive field sizes. The primary focus of our feature extraction backbone networks is on ResNet [26] and ResNet-RS-based [27] architectures. These architectures include identity mapping based on residual connections. Compared to the original ResNet the ResNet-RS extends this approach by enhancements such as random skip connections and residual connections to aggregate current feature maps with a randomly selected subset of previous feature maps. The integration of random skip connections serves to augment the learning capabilities of the CNN and diversify the learned representations. Specifically, the ResNet50, ResNet50-RS, ResNet101, ResNet101-RS, ResNet152, and ResNet152-RS variations were chosen as the backbone net for the Deeplabv3+. A binary segmentation problem was created for the model to pre-identify suitable landing sites. Only one class of the two possibilities can be assigned to one pixel of the network's output for this binary problem.

All versions of the network output a probability distribution based on a sigmoid function. The sigmoid function is typical for binary segmentation or classification tasks. The tensor $\mathbf{x} \in \mathbb{R}^{H \times W \times C}$ represents the input (camera and depth image), where H is the height, W is the width, and C is the number of input channels. With $\mathbf{x}$, the CNN receives the original grayscale 2D image data. For better training results, every input depth image was rescaled by min/max normalization according to Eq. 1.

$$(1) \qquad \mathbf{x}_{scaled} = \frac{\mathbf{x}_{unscaled} - \min(\mathbf{x}_{unscaled})}{\max(\mathbf{x}_{unscaled}) - \min(\mathbf{x}_{unscaled})}$$

It should be noted that the received high-resolution depth image from our AI-based LiDAR / Camera data fusion is already scaled to relative floating-point values $f \in [0, 1]$. For better visualization, the notation of Papernot et al. (2016) was used, where $\mathbf{F}_1, ..\mathbf{F}_n$ denotes the different layers of a CNN [28]. The complete CNN with its last sigmoid function is represented by $\mathbf{F}(x)$. The output matrix $\mathbf{y}$ is described by $\mathbf{F}(x)$ in Eq. 2 and has the shape of $\mathbf{x} \in \mathbb{R}^{H \times W}$. It depends on the output of the network's last layer activation function $\mathbf{Z}(\mathbf{x})$.

$$(2) \qquad \begin{aligned} \mathbf{F} &= sigmoid \circ \mathbf{F}_n \circ \mathbf{F}_{n-1} \circ ... \circ \mathbf{F}_1 \\ \mathbf{F}(\mathbf{x}) &= sigmoid(\mathbf{Z}(\mathbf{x})) =: \mathbf{y} \end{aligned}$$

3.3. Dataset details

For training the GAN of our AI-based LiDAR/Camera data fusion, we created a dataset comparable to the current Astrone KI project conditions. With CamSim [29] developed by Astos Solutions, a Digital Elevation Map (DEM) inspired by the comet 67P/Churyumov-Gerasimenko's surface, with a resolution of 0.05 m/pixel was generated. Subsequently, the open-source 3D computer graphics software Blender [30] was used to render the grayscale 2D images and the corresponding flash-LiDAR data in the form of depth images.

(a) Camera image (b) Camera image with shadows (sun azimuth of 45°)

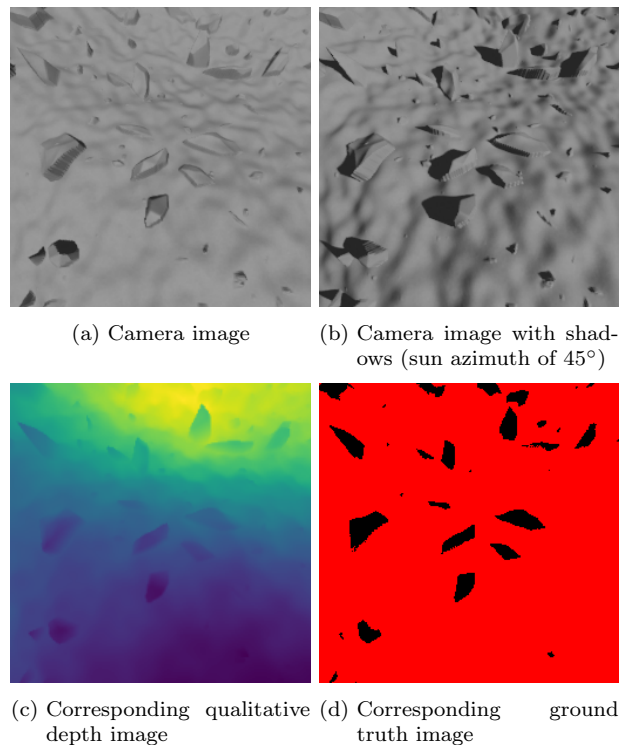(c) Corresponding qualitative depth image (d) Corresponding ground truth image

FIG 4. Generated grayscale 2D image, corresponding qualitative depth image, and ground truth for the AI-based landing site detection.

An artificially generated dataset was used to train and validate the AI-based landing zone detection. This dataset was introduced by Suwinski et al. (2023) [14]. Therefore, the focus will be solely on the process of generating data for the landing site. The generation of the simulated surface's DEM is based on the approach by Schimpf et al. (2022) [16]. Also, this approach generates the necessary ground truth data or labels for landing-site estimation. Slope, roughness, rocks, boulders, and craters are concerned to determine if an area is suitable for landing. The processing was optimized for our purposes. The actual camera images

with resulting shadows of a sun azimuth of $\pm45°$ in $15°$ steps and corresponding depth images were then rendered with Blender. Fig. 4 shows the input and ground truth data for the supervised learning training of the CNNs. Red areas are suitable landing spots. Within the scope of the Astrone KI project, we will use CamSim in the future for the total data generation process for all AI-based solutions. Instead of just using a DEM from CamSim, it will generate the required image data right away.

4. EXPERIMENTS AND RESULTS

4.1. Overview and metrics

This paper provides only an overview of the AI-based LiDAR/camera data fusion [7]. Therefore, we focus on the validation of the landing site detection.
All CNN versions have been trained for 25 Epochs with 3060 iterations each. The batch size was set to 25, and Adam optimizer with a learning rate of $l = 5 * 10^{-5}$, $\beta_1 = 0.9$, and $\beta_2 = 0.999$ were used. To counter overfitting $L2$-regularization with $\lambda = 10^{-6}$ was applied. Furthermore, for every CNN configuration, the binary cross-entropy was used as a loss function. All networks were trained with 76.500 and tested with 8.500 samples. An NVIDIA RTX 3090 GPU and a Ryzen 9 5950x CPU were utilized for training and testing.

To evaluate the performance of each CNN version, the following metrics were used, which are described in Eq. 3. These metrics produce quantitative results by comparing the ground truth $\mathbf{y}$ with the network's predicted output $\hat{\mathbf{y}}$. Higher values for the precision mean the model makes many true positive (TP) and fewer false positive (FP) classifications. A higher recall indicates that the network makes more true positive (TP) and fewer false negative (FN) predictions. The F1-score takes both precision and recall into account. Higher values are better here, too. The higher values of the IoU describe a better similarity between ground truth and the prediction.
It is important to note that the average values of these metrics are calculated based on the number of test samples n. Further, a scaling factor 100 was applied to precision, recall, and IoU for better visualization.

$$\text{(3a)} \qquad precision = \frac{100}{n} \cdot \sum_{k=1}^{n} \frac{TP_k}{TP_k + FP_k}$$

$$\text{(3b)} \qquad recall = \frac{100}{n} \cdot \sum_{k=1}^{n} \frac{TP_k}{TP_k + FN_k}$$

$$\text{(3c)} \qquad F1 = 2 \cdot \frac{precision \cdot recall}{precision + recall}$$

$$\text{(3d)} \qquad IoU = \frac{100}{n} \cdot \sum_{k=1}^{n} \frac{|\mathbf{y}_{k,true} \cap \mathbf{y}_{k,pred}|}{|\mathbf{y}_{k,true} \cup \mathbf{y}_{k,pred}|}$$

4.2. Validation and Testing

The test portion of our artificially generated dataset was used for validation and testing purposes. For all experiments, we trained and tested with different illumination conditions. The change of the sun azimuth between $\pm45°$ within $15°$ steps created varying amounts of shadows on the surface visible in the generated grayscale 2D images. To assess the performance of Deeplabv3+, we tested it with different configurations that varied in their backbone net. The original ResNet was compared with ResNet-RS. Deep neural networks are often prone to overfitting, especially when working with an artificially generated dataset. Therefore, the number of layers were limited to 50, 101, and 152 for both backbone net architectures. In addition, limiting the number of layers helps to balance the computational effort since deeper networks require more computational power for inference.

TAB 1. Validation of semantic segmentation on the artificially generated dataset with 2D image input data, with backbone nets in brackets

CNN	Prec.	Rec.	F1	IoU
Deeplabv3+ (ResNet50)	98.85	91.81	95.20	61.26
Deeplabv3+ (ResNet101)	98.42	91.20	94.65	58.93
Deeplabv3+ (ResNet152)	98.87	91.58	95.09	60.28
Deeplabv3+ (ResNet50-RS)	98.60	92.34	95.36	65.23
Deeplabv3+ (ResNet101-RS)	98.48	92.30	95.28	64.09
Deeplabv3+ (ResNet152-RS)	98.23	92.64	95.35	64.12

TAB 2. Validation of semantic segmentation on the artificially generated dataset with 2D image input data corresponding depth image input data, with backbone nets in brackets

CNN	Prec.	Rec.	F1	IoU
Deeplabv3+ (ResNet50)	98.46	92.2	95.22	62.50
Deeplabv3+ (ResNet101)	97.99	92.80	95.33	64.46
Deeplabv3+ (ResNet152)	98.96	91.83	95.28	61.73
Deeplabv3+ (ResNet50-RS)	99.14	92.63	95.78	67.45
Deeplabv3+ (ResNet101-RS)	98.54	92.93	95.66	66.81
Deeplabv3+ (ResNet152-RS)	98.33	92.62	95.39	64.15

(a) ResNet50   (b) ResNet101

(c) ResNet152   (d) ResNet50-RS (best)
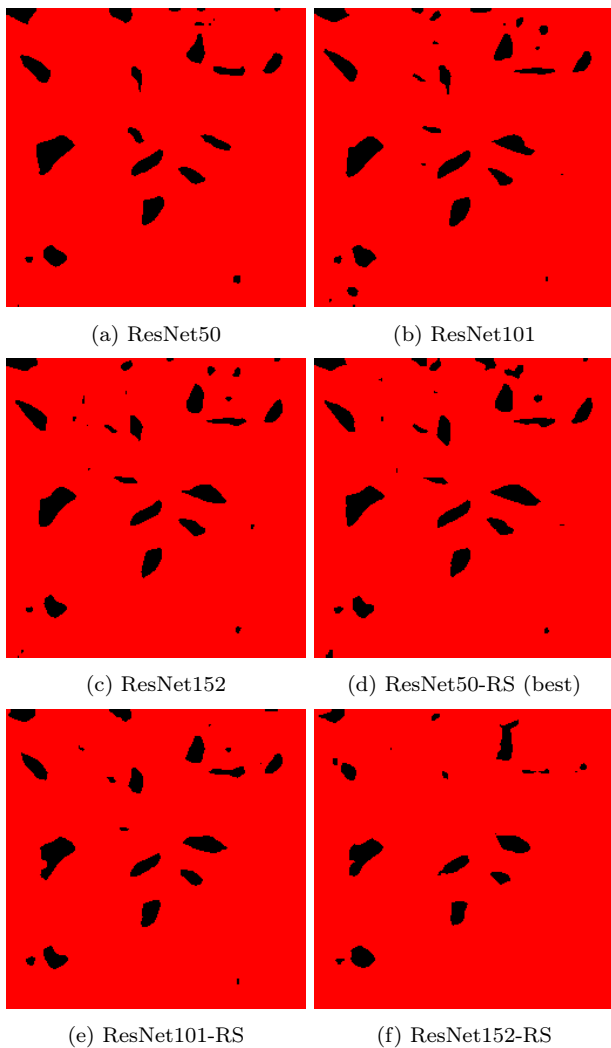
(e) ResNet101-RS   (f) ResNet152-RS

FIG 5. Visualized landing site predictions for different backbone nets with a grayscale 2D image (Fig. 4a) and corresponding depth (Fig. 4c) image as input. Red-marked areas are classified as suitable for landing.

(a) Camera image (45°)   (b) Qualitative depth image

(c) ResNet50-RS   (d) Corresponding ground truth image

FIG 6. Vizualized landing site prediction with a crater of the best performing Deeplabv3+ version with ResNet50-RS backbone. Red-marked areas are classified as suitable for landing.

In a first experiment, we trained all configurations with just a grayscale 2D image as input, with no additional depth information, and tested the Deeplabv3+ variants' ability to detect suitable landing sites. Tab. 1 shows the results of this testing. According to these results, the performance of the CNN variant does not necessarily increase with the number of backbone net layers. In some cases, it even decreases. The ResNet50-RS-based network performed the best with the highest IoU. Fig. 7 in appendix A includes a visualization of misclassifications compared to the ground truth (Fig. 4d) for every Deeplabv3+ configuration.

The high-resolution flash-LiDAR information as a depth image was added to the CNN's input for the next test. An overall performance improvement could be achieved here. Again, the CNN with the ResNet50-RS backbone achieved the highest IoU of 67.45. Fig. 5a - 5f depict the output for all variants. The visualized output Fig. 5d is the closest to the corresponding ground truth (Fig. 4d). It was possible
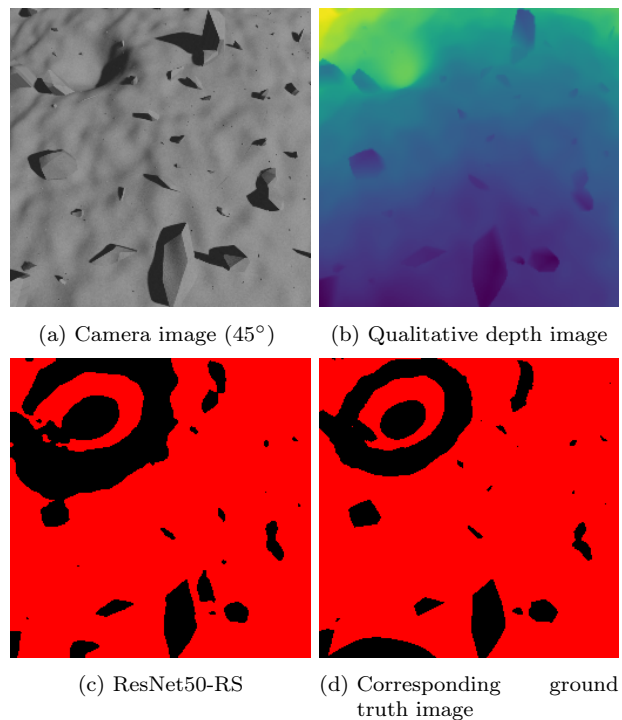
to detect small stones as well as larger rocks and classify these areas as unsuitable for landing. Fig. 6c shows one example where the best-performing network (ResNet50-RS backbone) must detect a crater on the simulated asteroid's surface. It was possible for the network to predict the crater and the areas with strong slope changes around it. This task is harder because objects like craters with strong slope changes are less frequent in our training data set.

5. LIMITATION AND FUTURE WORK

It should be noted again that an artificially generated dataset was used for training. Even though an artificial dataset can represent reality to some degree, it typically has a limited range of variation compared to the real world. A neural network can filter some noise if it has been trained with data containing this noise. However, artificially generated datasets contain no noise or may not accurately reflect it. Therefore, the network will have problems processing real-world data.

Due to the unavailability of ground truth data, an important step in the future is to improve our data generation process further and create more realistic training and test data, which is essential for performance and robustness in a real-world environment. Additionally, a transfer learning approach with CamSim data will be used to optimize the training strategy, enhancing the performance and robustness in the scope of our project. In this paper, we have concentrated on a CNN-only approach. Other neural network architec-

tures may perform better in some scenarios, especially with high-resolution data. Therefore, our future work will focus on testing vision transformer approaches in combination with CNN-based approaches.

6. CONCLUSION

This paper presented the AI Mapping part of the Astrone KI navigation concept. We propose an AI-based approach to detect and pre-identify suitable landing sites for a small vehicle operating close to the surface of an SSSB. Different versions of the Deeplabv3+ CNN were trained and validated using an artificially generated dataset of the surfaces of SSSBs. Data with different sun positions were created to simulate changes in local illumination during a real mission. The results show adding high-resolution depth images can increase the performance of the segmentation process for the lading-site detection instead of just relying on camera images. Our method was able to detect objects like stones and rocks. Also, areas dangerous for landing around craters with great slopes were roughly recognized in this first attempt.

Additionally, this paper gave an overview of an AI-based approach to increase the resolution of low-resolution 3D terrain data by data fusion with a single monocular 2D grayscale image. This part of the AI Mapping made it possible to use high-resolution depth images for the landing site detection.

The presented solution shows the potential for AI-based approaches as part of guidance and navigation applications on irregular SSSBs.

7. ACKNOWLEDGEMENT

Contact address:

alexander.liesch@tu-dresden.de

References

[1] J Veverka, B Farquhar, M Robinson, P Thomas, S Murchie, A Harch, PG Antreasian, SR Chesley, JK Miller, WM Owen Jr, et al. The landing of the near-shoemaker spacecraft on asteroid 433 eros. Nature, 413(6854):390–393, 2001.

[2] Karl-Heinz Glassmeier, Hermann Boehnhardt, Detlef Koschny, Ekkehard Kührt, and Ingo Richter. The rosetta mission: flying towards the origin of the solar system. Space Science Reviews, 128:1–21, 2007.

[3] CT Russell and CA Raymond. The dawn mission to vesta and ceres. The dawn mission to minor planets 4 Vesta and 1 Ceres, pages 3–23, 2012.

[4] Makoto Yoshikawa, Junichiro Kawaguchi, Akira Fujiwara, and Akira Tsuchiyama. Hayabusa sample return mission. Asteroids IV, 1(397-418):1, 2015.

[5] M Martin, F Belien, B Liu, J Olucak, F Schimpf, T Brüggemann, A Falke, V Sadovski, V Chernykh, K Janschek, et al. Astrone–gnc for enhanced surface mobility on small solar system bodies. In 11 th International ESA Conference on Guidance, Navigation & Control Systems, 2021.

[6] M Martin, E Caroselli, J Olucak, S Busi, W Fichter, B Liu, A Liesch, P Suwinski, V Chernykh, and K Janschek. Pioneering the small bodies frontiers: The key enabling technologies for autonomous precise mobilitys. In 12 th International Conference on Guidance, Navigation & Control Systems (GNC), 2023.

[7] A Liesch, P. Suwinski, B. Liu, V. Chernykh, and K. Janschek. Ai-based lidar / camera data fusion to enable high-resolution 3d surface reconstruction for autonomous asteroid exploration mission. AAS/AIAA Astrodynamics Specialist Conference, Big Sky, MT, Aug 13-17, 2023. Paper AAS-422.

[8] Go Ono, Fuyuto Terui, Naoko Ogawa, Shota Kikuchi, Yuya Mimasu, Kent Yoshikawa, Hitoshi Ikeda, Yuto Takei, Seiji Yasuda, Kota Matsushima, et al. GNC strategies and flight results of Hayabusa2 first touchdown operation. Acta Astronautica, 174:131–147, 2020.

[9] DS Lauretta, SS Balram-Knutson, E Beshore, WV Boynton, C Drouet d'Aubigny, DN DellaGiustina, HL Enos, DR Golish, CW Hergenrother, ES Howell, et al. OSIRIS-REx: sample return from asteroid (101955) Bennu. Space Science Reviews, 212:925–984, 2017.

[10] Patrick Michel, Michael Kueppers, Holger Sierks, Ian Carnelli, Andy F Cheng, Karim Mellab, Mikael Granvik, Antti Kestilä, Tomas Kohout, Karri Muinonen, et al. European component of the AIDA mission to a binary asteroid: Characterization and interpretation of the impact of the DART mission. Advances in Space Research, 62(8):2261–2272, 2018.

[11] Bangshang Liu, Vasko Sazdovski, Valeriy Chernykh, and Klaus Janschek. Flash lidar aided-inertial navigation on surfaces of small solar system bodies using error state kalman filtering. AAS/AIAA Astrodynamics Specialist Conference, Aug 8-12, 2021. Paper AAS 21-752.

[12] R. W. Gaskell, O. S. Barnouin-Jha, D. J. Scheeres, A. S. Konopliv, T. Mukai, S. Abe,

J. Saito, M. Ishiguro, T. Kubota, T. Hashimoto, J. Kawaguchi, M. Yoshikawa, K. Shirakawa, T. Kominato, N. Hirata, and H. Demura. Characterizing and navigating small bodies with imaging data. 43(6):1049–1061. ISSN: 1945-5100. DOI: 10.1111/j.1945-5100.2008.tb00692.x.

[13] M. M. Al Asad, L. C. Philpott, C. L. Johnson, O. S. Barnouin, E. Palmer, J. R. Weirich, M. G. Daly, M. E. Perry, R. Gaskell, E. B. Bierhaus, J. A. Seabrook, R. Espiritu, H. Nair, C. Ernst, R. T. Daly, M. C. Nolan, H. L. Enos, and D. S. Lauretta. Validation of Stereophotoclinometric Shape Models of Asteroid (101955) Bennu during the OSIRIS-REx Mission. 2(2):82, 2021. ISSN: 2632-3338. DOI: 10.3847/PSJ/abe4dc.

[14] Patrick Suwinski, Alexander Liesch, Bangshang Liu, Valerij Chernykh, and Klaus Janschek. AI-based pre-processing for navigation on significantly unstructured planetary surfaces. Deutscher Luft- und Raumfahrt Kongress, Stuttgart, Germany, Sep 19-21, 2023.

[15] Zexiao Xie, Xiaoxuan Yu, Xiang Gao, Kunqian Li, and Shuhan Shen. Recent advances in conventional and deep learning-based depth completion: A survey. IEEE Transactions on Neural Networks and Learning Systems, pages 1–21, 2022. DOI: 10.1109/TNNLS.2022.3201534.

[16] Fabian Schimpf, Jan Olucak, and Walter Fichter. Robust landing site detection for flight over small solar system bodies. In AIAA SCITECH 2022 Forum, page 0955, 2022.

[17] MGGT Taylor, N Altobelli, BJ Buratti, and M Choukroun. The rosetta mission orbiter science overview: the comet phase. Philosophical Transactions of the Royal Society A: Mathematical, Physical and Engineering Sciences, 375(2097):20160262, 2017.

[18] Ian J. Goodfellow, Jean Pouget-Abadie, Mehdi Mirza, Bing Xu, David Warde-Farley, Sherjil Ozair, Aaron Courville, and Yoshua Bengio. Generative Adversarial Nets. DOI: 10.48550/arXiv.1406.2661, http://arxiv.org/abs/1406.2661.

[19] Yu Tao, Jan-Peter Muller, Siting Xiong, and Susan J. Conway. MADNet 2.0: Pixel-Scale Topography Retrieval from Single-View Orbital Imagery of Mars Using Deep Learning. 13(21):4220. ISSN: 2072-4292. DOI: 10.3390/rs13214220.

[20] Yang Liu, Yexin Wang, Kaichang Di, Man Peng, Wenhui Wan, and Zhaoqin Liu. A Generative Adversarial Network for Pixel-Scale Lunar DEM Generation from High-Resolution Monocular Imagery and Low-Resolution DEM. 14(21):5420. ISSN: 2072-4292. DOI: 10.3390/rs14215420.

[21] Riccardo La Grassa, Ignazio Gallo, Cristina Re, Gabriele Cremonese, Nicola Landro, Claudio Pernechele, Emanuele Simioni, and Mattia Gatti. An Adversarial Generative Network Designed for High-Resolution Monocular Depth Estimation from 2D HiRISE Images of Mars. 14(18):4619. ISSN: 2072-4292. DOI: 10.3390/rs14184619.

[22] Olaf Ronneberger, Philipp Fischer, and Thomas Brox. U-net: Convolutional networks for biomedical image segmentation. In Medical Image Computing and Computer-Assisted Intervention–MICCAI 2015: 18th International Conference, Munich, Germany, October 5-9, 2015, Proceedings, Part III 18, pages 234–241. Springer, 2015.

[23] Huimin Huang, Lanfen Lin, Ruofeng Tong, Hongjie Hu, Qiaowei Zhang, Yutaro Iwamoto, Xianhua Han, Yen-Wei Chen, and Jian Wu. UNet 3+: A Full-Scale Connected UNet for Medical Image Segmentation, Apr. 2020. http://arxiv.org/abs/2004.08790.

[24] Phillip Isola, Jun-Yan Zhu, Tinghui Zhou, and Alexei A. Efros. Image-to-Image Translation with Conditional Adversarial Networks, Nov. 2018. http://arxiv.org/abs/1611.07004.

[25] Liang-Chieh Chen, Yukun Zhu, George Papandreou, Florian Schroff, and Hartwig Adam. Encoder-decoder with atrous separable convolution for semantic image segmentation. In Proceedings of the European conference on computer vision (ECCV), pages 801–818, 2018.

[26] Kaiming He, Xiangyu Zhang, Shaoqing Ren, and Jian Sun. Deep residual learning for image recognition. In Proceedings of the IEEE conference on computer vision and pattern recognition, pages 770–778, 2016.

[27] Irwan Bello, William Fedus, Xianzhi Du, Ekin Dogus Cubuk, Aravind Srinivas, Tsung-Yi Lin, Jonathon Shlens, and Barret Zoph. Revisiting resnets: Improved training and scaling strategies. Advances in Neural Information Processing Systems, 34:22614–22627, 2021.

[28] Nicolas Papernot, Patrick McDaniel, Xi Wu, Somesh Jha, and Ananthram Swami. Distillation as a defense to adversarial perturbations against deep neural networks. In 2016 IEEE symposium on security and privacy (SP), pages 582–597. IEEE, 2016.

[29] J Eggert, S Weikert, and I Kossev. Imaging sensor emulation and dynamics simulation for pil/hil.

[30] Blender Online Community. Blender - a 3D modelling and rendering package. Blender Foundation, Stichting Blender Foundation, Amsterdam, 2018.

A. APPENDIX

(a) ResNet50   (b) ResNet101   (c) ResNet152

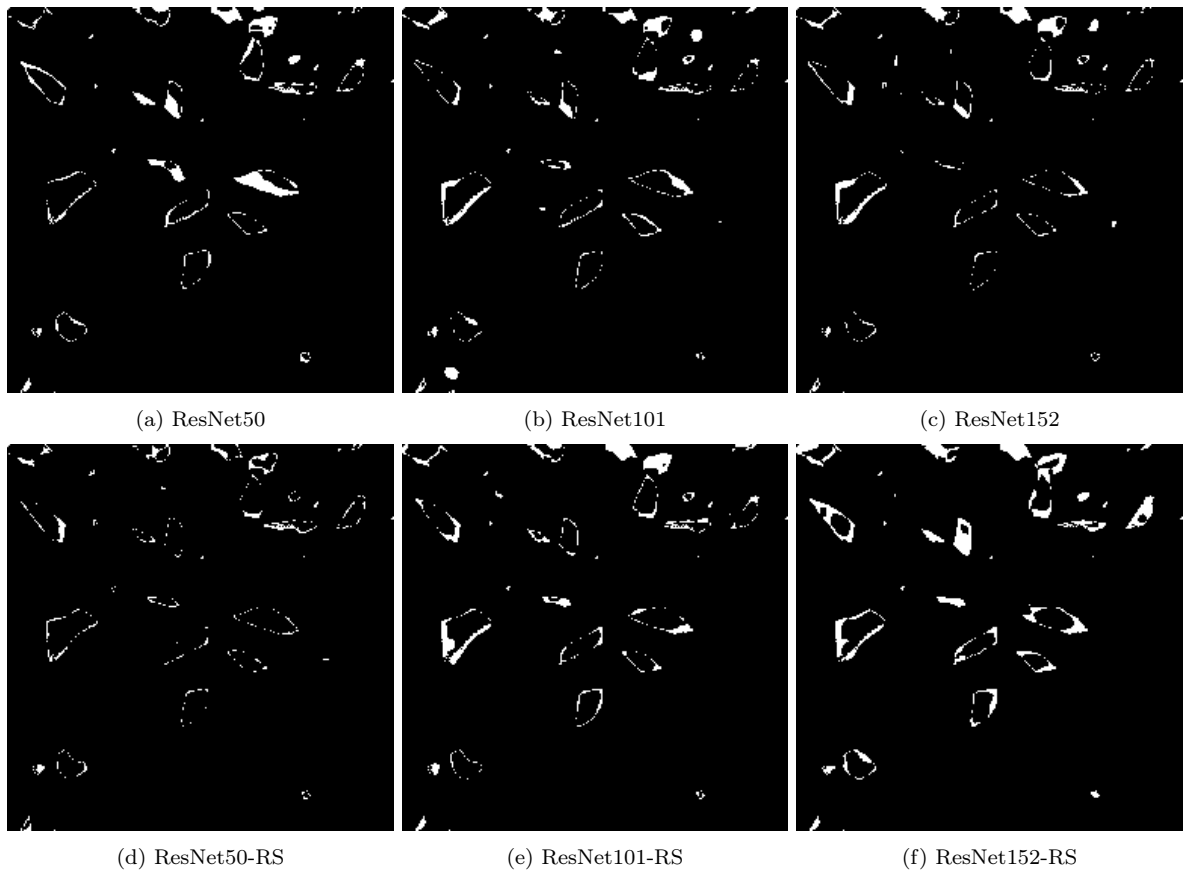(d) ResNet50-RS   (e) ResNet101-RS   (f) ResNet152-RS

FIG 7. Visualized misclassifications (white) of the Deeplabv3+ with different backbone net configurations for the output shown in Fig. 5.